LJMU Research Online

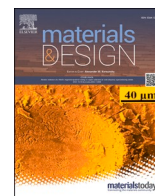**Yang, X, Gibbons, GJ, Tanner, DA, Li, Z, Wilson, P, Williams, MA and Kotadia, HR**

 Scan strategy induced microstructure and consolidation variation in the laser-powder bed fusion (L-PBF) additive manufacturing of low alloy 20MnCr5 steel

http://researchonline.ljmu.ac.uk/id/eprint/21756/

Article

For more information please contact researchonline@ljmu.ac.uk

Scan strategy induced microstructure and consolidation variation in the laser-powder bed fusion (L-PBF) additive manufacturing of low alloy 20MnCr5 steel

Xinliang Yang [a,b], Gregory J. Gibbons [a], David A. Tanner [c], Zushu Li [a,*], Paul Wilson [a], Mark A. Williams [a], Hiren R. Kotadia [a,d,*]

[a] *WMG, University of Warwick, Coventry CV4 7AL, UK*
[b] *BCAST, Brunel University London, Uxbridge UB8 3PH, UK*
[c] *Bernal Institute & School of Engineering, University of Limerick, Limerick, V94 T9PX, Ireland*
[d] *School of Engineering, Liverpool John Moores University, Liverpool L3 5UX, UK*

ABSTRACT

The paper focuses on the effect of the scanning strategies on the microstructural evolution, defect formation, and macro-hardness performance of laser-powder bed fusion (L-PBF) produced samples of low alloy 20MnCr5 steel. Respect to the scanning strategies, advanced characterization techniques were employed to study (i) as-built microstructure, (ii) inclusion size and distribution, and (iii) details of compositional variation around porosity and within the build. Microstructural characterization shows that the chessboard scanning strategy can provide a favorable microstructure for the improvement of mechanical performance. However, macro-hardness results show a lower mechanical performance compared to the linear scanning strategy samples, which is contradicted by the improved microstructure. Experimental results reveal that the chessboard scanning strategy promotes the oxidation reaction and *in-situ* oxide (SiO_2) formation in L-PBF, which leads to significant defect formation due to the excessive thermal profile from the overlap of the laser. This has been validated through finite element analysis and thermodynamic computation. The advantages of microstructural improvement using the chessboard strategy can only be realized with strict control of the metallurgical quality during the L-PBF process. Thermal profile optimization and oxygen elimination during the L-PBF process could be critical for the improved metallurgical quality and superior mechanical performance of the as-built components.

1. Introduction

In the last decade, the scientific and industrial community has shown tremendous interest in Additive Manufacturing (AM) technology. AM offers potential advantages in comparison to the conventional manufacturing methods, specifically, the capability to create complex shaped products with greater precision and without tooling, less material wastage, significant light weighting, while maintaining strength and structural integrity with a shorter supply chain [1–3]. For instance, AM is currently being used to produce prototype and real-life products in the industrial applications of aerospace, automotive, energy, defense, sports, and biomedicine [4]. Metallic material grades of titanium (e.g., Ti64 [5]), nickel (e.g., IN718 [6]), stainless steel (e.g., 316L [7]) and aluminum (e.g., AlSi10Mg [8]) alloys are examples of those used in AM.

Laser Powder Bed Fusion (L-PBF) is a particular AM technique using a high energy laser beam to melt and fuse metallic powders in a layer-by-layer pattern. The microstructure produced through the L-PBF process often consists of columnar grains with a specific texture in the building (vertical) direction due to the repetitive heating and cooling cycles [1,3,7]. During the nature of this process, the growth of individual phases is dependent on the local thermal field [9], and the presence of solute and nucleant particles [3,9]. Literature on various metallic alloys have shown that L-PBF microstructural features (e.g., phase constitution, grain size, non-metallic inclusion, and porosity) and properties (e.g., strength, ductility, fatigue, corrosion) can be tailored by adjusting their processing parameters such as the laser power, scanning speed, and the scan vector orientation [10–14]. Therefore, it is essential to optimize these processing parameters for safety–critical components fabricated

---

by AM.

Currently, researchers have been exploring two main approaches of refining microstructure, namely, (i) materials modification by using inoculants e.g., TiN [15], TiB₂ [16], Al₃Sc [17], LaB₆ [18] and solute elements e.g., Si, Cu, Ni [19] to influence grain size and growth and (ii) variation of scanning strategy to alter local heat transfer conditions to change grain growth [8,14,20,21]. Amongst these two approaches, scanning strategy is more practical to implement with commercially available powder feedstock. This combinatorial strategy can influence heat transfer, melt pool convection, and local solidification rate. Previous studies [22,23] on Ni-based superalloys (Inconel 718 and IN738LC) have shown that a spatially controlled crystallographic texture and elastic anisotropy can be achieved. Marattukalam et al. [24] studied a 316L alloy through scanning strategy optimization, which significantly influenced the size of austenite cells and grains and led to improved mechanical properties. Haines et al. [25] studied Fe-Si soft magnetic alloys and demonstrated that scanning strategies can alter grain morphology (columnar to equiaxed) and realize a different response to the annealing process at 1200 °C. Moreover, other studies demonstrated that scanning strategy can help to limit solute segregation on High Angle Grain Boundaries (HAGBs) and reduce the thermal stresses which led to hot cracking [26]. The materials summarized in this paragraph are mainly casting friendly alloys. However, there is very limited research and knowledge on the influence of scanning strategy on materials such as low alloy steels, which were specifically designed, and mass produced into distinct profiles, by conventional continuous casting and thermo-mechanical processing.

Widespread implementation of AM in metals requires low cost and robust materials such as low alloy steels, which offer comprehensive mechanical performance, including strength, ductility, toughness, and wear resistance, while maintaining a low cost. Several low-alloy steels have been studied using L-PBF, including 20MnCr5 [27], 24CrNiMo [28], AISI 4130 [29], and 4340 [30]. Most of these studies focused on printability and the role of initial processing parameters (laser power and scanning speed) on microstructure and mechanical properties. As these steel grades are exclusively designed for conventional steel-making, the inclusion/oxide metallurgy (interaction of the oxygen and liquid steel) are expected to be different in the L-PBF process than in the conventional steelmaking.

Recent experimental research has shown that metal powders have a tendency to pick up oxygen during their manufacturing, handling, and processing. For instance, our previous work [31,32] on 316L stainless steel revealed the role of oxides on liquid permeability during the solidification and alteration of chemical composition of powder by depleting solute elements to oxides. Work also highlighted how inclusion agglomeration changes solidification characteristics. Song et al. [33] revealed that increasing the inclusion contents induced by different purities of protective gas on AISI 420 stainless steel has an impact on the build quality of components. Eo et al. [34] conducted a detailed quantitative analysis that demonstrated the relationship of inclusion size and volume on the variation of the mechanical properties using 316L stainless steel. Deng et al. [35] examined the oxide inclusions in 316L steel by considering powder manufacturing, storage, and processing. Nevertheless, there are still very few studies on powder oxidation and defect formation of low alloy steel grades with respect to scanning strategies. Therefore, detailed experimental and characterization studies are required to confirm the mechanisms and establish the condition under which oxides are formed and quantify the influence of defect formation.

This research does not cover the relationship between L-PBF processing parameters – and tensile properties, as such information has already been included in the described literature in the preceding paragraphs. Instead, this work aims to reveal the influence of the scanning strategy on the metallurgical characteristics of the as-built parts. A martensitic 20MnCr5 gear steel was selected as the model alloy to study the effect of varying scanning strategies on the microstructural evolution, defect formation, consolidation, and its impact on the mechanical response (macro-hardness) of a low alloy steel in the L-PBF process. To achieve this goal, various advanced characterization techniques are employed to study microstructural evolution, chemical composition of inclusion / oxides, and defects of as-fabricated samples. The study examines the thermal fields induced by energy input, scanning time and temperature gradient with respect to the scanning strategy by using a finite element model. Experimental results and thermodynamic analysis confirmed the oxide species and their role on porosity formation. The research outcomes provide an insight into the relationship of materials-processing parameters in the L-PBF process by focusing on a low alloy steel, which represents a steel grade that is sensitive to the presence of oxygen during manufacture.

2. Experimental methods

2.1. Materials

A low-alloy case-hardening steel 20MnCr5 powder from Phoenix Scientific Industrial Ltd. (PSI), UK (Fig. 1) was used in this study to understand the effect of scan strategies on the oxidation of low alloy steel grades. The nominal chemical composition of this Ar-gas atomized steel powder is presented in Table 1. The particle size distribution calculated using a microscopy imaging approach is shown in Fig. 1(b). The D_{10}, D_{50} and D_{90} sizes are 12.5 μm, 25.6 μm and 73.3 μm, respectively. The upper size is limited to 150 μm by sieve separation.

2.2. Laser-powder bed fusion (L-PBF) and scan strategies

The L-PBF process was performed using an EOSintM 280 L-PBF 3D printer (EOS GmbH, Germany) in an argon atmosphere, fabricating cuboid specimens (14 (w) × 14 (b) × 14 (h) mm³) to study microstructure and defect formation. The protective atmosphere of 99.998% (4.8 N) purity argon was stated in the equipment technical documentation [37] and acquired from BOC UK (with less than 20 ppm impurity of O_2, H_2O, and N_2). The flow rate of the Ar gas was 10 L/min during the L-PBF process.

The volumetric energy density (VED), an auxiliary factor combining the processing parameters with the layer thickness, is often used to normalize the input energy [38]. It is given as:

$$E = \frac{P}{v \bullet h_d \bullet t_l} \tag{1}$$

where, E is the volumetric energy in J/mm³, P is the laser power in W, v is the scanning velocity in mm/s, h_d is the hatch distance in mm, and t_l is the layer thickness in mm. An initial processing parameter selection was referred to the study of the L-PBF processed 16MnCr5 gear part [39]. In their energy density to specimen density relationship study, the energy densities of 70 J/mm³ and above resulted in a 99% as-built density uniformly in both sections perpendicular to building direction (XY plane) and sections parallel to building direction (XZ plane). Based on that, the optimized L-PBF printing parameters used for 20MnCr5 sample fabrication are listed in Table 2, which provided a volumetric energy density of 74 J/mm³.

In this study, typical linear and chessboard scan strategies were utilized to conduct the L-PBF process. The detailed geometry and laser track angles are presented in Fig. 2. To reveal the influence of scan strategy, the path frame of reference was kept constant for each layer added (rather than the machine default 67° rotation between adjacent layers). Although individual factors of the scan strategy, scan pattern, rotation angle between layers, multiple scanning in one layer, and/or multiple laser sources, have their unique influence on the build characteristics, the scan pattern is normally considered as the major variable which has been extensively studied [23,40–44]. Based on that, the scan pattern was selected to form a strict comparative study. In total 9
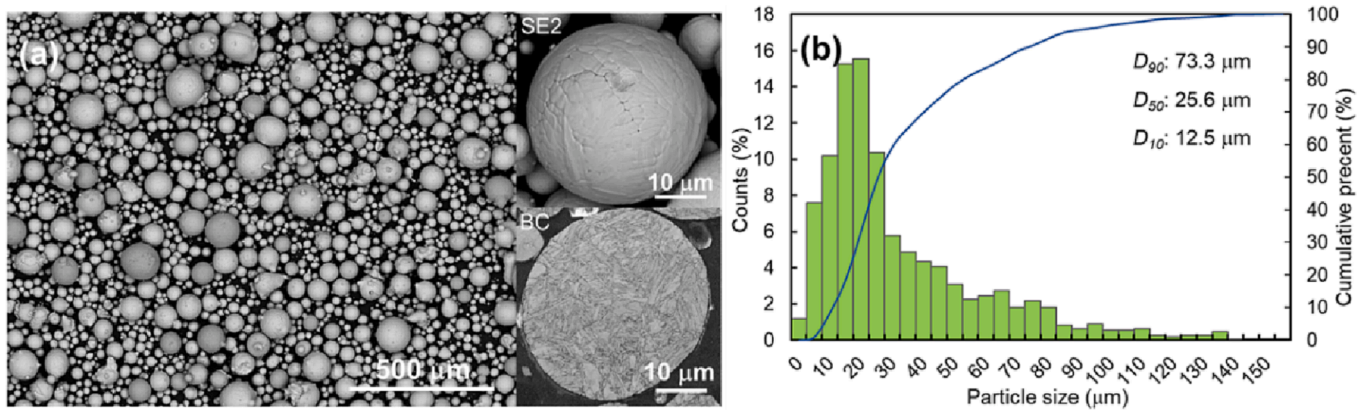
Fig. 1. The characterization of as received 20MnCr5 steel powder (a) powder morphology in Secondary Electron (SE2) contrast and cross section of the powder with martensitic structure in Band Contrast (BC) signal; and (b) statistical analysis of the particle size distribution.

Table 1
Nominal chemical composition of the as received 20MnCr5 steel powder.

wt.%	Cr	Mn	Si	Mo	Ni	C	Fe
As received	1.25	1.20	0.29	0.15	0.14	0.108	Bal.
DIN EN 10084: 2008–06 [36]	1.00–1.30	1.10–1.40	Max. 0.40	–	–	0.17–0.22	Bal.

Table 2
L-PBF processing parameters for 20MnCr5 powder build.

Laser power	Scan speed	Laser spot size	Hatch distance	Layer thickness
280 W	950 mm/s	70 μm	100 μm	40 μm

cuboids for each scan strategy were built in the L-PBF process. In the chessboard strategy, a 7 × 7 square array was designed in each sample build with dimension of 2 mm × 2 mm for each square (Fig. 2(b)). The default scan vector orientation settings in the EOSintM 280 operation interface were selected as indicated in Fig. 2. The scan vectors of the neighboring squares of the chessboard strategy were set to be variable, with some at 45° and some at 77° to the X-axis (layer recoating direction) (Fig. 2(b)).

2.3. Materials characterization

The cuboid samples of 20MnCr5 fabricated by the two scan strategies

were removed from the steel substrate plate using the wire electric discharge machining method. These as-built samples were subjected to Archimedes' density measurement according to ASTM B962 [45], and each sample was measured 3 times. These cuboids were then sectioned on transverse (XY plane) and longitudinal (XZ plane) parallel to the build direction (Z). The sectioned samples were prepared through a standard metallographic procedure with a final vibration polish using Buehler metallography techniques [46]. The polished samples were etched using Nital (1% HNO_3) for 3 min to unveil the microstructure.

2.4. Optical and scanning electron microscopy (SEM)

A VHX7000 optical microscope (Keyence UK) was utilized to quantify the porosity volume fraction. An Alicona Infinite focus microscope (Bruker Alicona, Austria) was used to measure surface roughness of the as-built samples at a magnification of 5X, following the ISO 4287 standard. A Jeol 7800F scanning electron microscope (SEM) (Jeol UK Ltd, UK) and a Verse FEI dual-beam focused ion beam (FIB) SEM (Thermo Fisher Scientific UK, UK) were employed to examine the microstructure
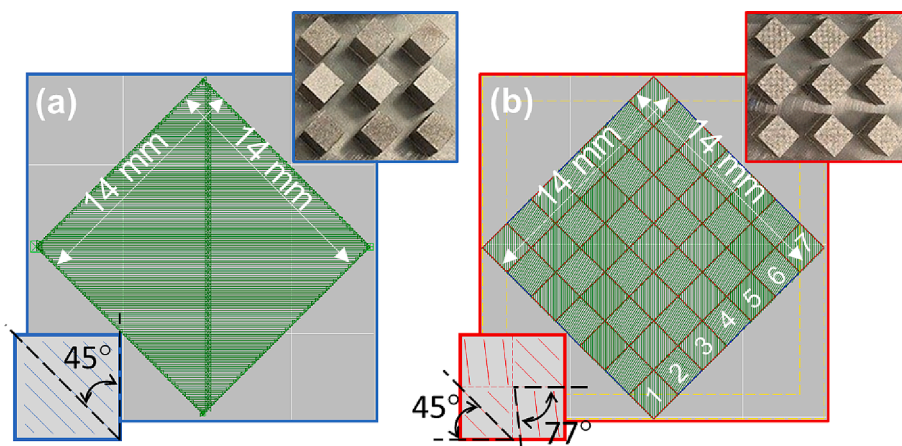

Fig. 2. The image of the as-build samples, laser track profile, the geometry for different scan strategies, and corresponding schematic illustrations (a) linear strategy, and (b) chessboard strategy.

of the as-built samples, during which both secondary electron (SE) and backscattered electron (BSE) images were acquired. The chemical analysis was carried out by energy-dispersive X-ray spectroscopy (EDS) (Oxford Instruments, UK) at 10 kV.

A Symmetry® EBSD detector (Oxford Instruments, UK) fitted within the Jeol 7800F SEM was used to acquire the crystallographic orientation information of the build at 20 kV, 1 μm step size, and ~ 2000 frame per second (fps) indexing rate. The Aztec software package (Oxford Instruments, UK) was used for the EBSD data analysis. The coordinate of the EBSD mapping was set as follow: x0 direction: X direction in the L-PBF process; y0 direction: Z direction in the L-PBF process; z0 direction: Y direction in the L-PBF process. The inverse pole figure (IPF) map is generated from z0 direction in the EBSD acquisition coordinate.

The statistical analysis of the porosity and inclusion distribution were conducted with ImageJ 1.49v software (National Institutes of Health, USA) using optical microscopy and SEM-BSE images, respectively. Also, note that some of the details about analysis are incorporated within the results section.

2.5. X-ray computed tomography (XCT)

XCT of the cuboid samples produced by linear and chessboard scan strategies was conducted using a Tescan UniTOM XL (Tescan Orsay Holding, Czech Republic). To acquire the best possible spatial resolution for the shape of the samples, the upper and lower halves of the sample were scanned separately and subsequently stitched together following image reconstruction in Panthera (Tescan Orsay Holding, Czech Republic). Each scan for the samples produced by linear and chessboard strategies used the same settings; with a voxel resolution of 5.8 μm, 180 kV, 15 W, and an exposure time of 2500 ms over 3837 projections at 3 frames per projection.

Porosity analysis of the samples was performed in Avizo 3D 2021.1 (Thermofisher Scientific UK, UK) using watershed segmentation, with subsequent manual adjustment to ensure greater accuracy of the extracted porosity. The extracted pores for both samples were subjected to label analysis to extract metrics of pore geometry and sample quality, including pore size (Length3D) and Volume (Volume3D). The total volume of pores and metal were also extracted and used to calculate the volume fraction of porosity for both samples.

2.6. Hardness test

Macro hardness was measured on the XY and XZ planes of the samples using a Wilson® VH3300 Vickers hardness tester (Buehler UK, UK) with a 50 kg force loading and 10 s dwell time. The indentation covered ~ 0.5 mm × 0.5 mm area, which is considered representable for revealing the mechanical response of a bulk material. Nine indentations were conducted in a 3 × 3 matrix on the testing planes of each sample. The indentations were separated from each other by 2 mm [47].

2.7 Theoretical analysis

2.7.1. Thermal field simulation

An Abaqus Finite Element Model was built with the AM Modeler Plugin in ABAQUS v2020 (Dassault Systems, France) to simulate the thermal field distribution during and after the build process. The detailed laser toolpath order of the chessboard strategy in the finite element simulation is presented in Fig. 3 [48]. Material property data as a function of temperature for the base plate and the build was sourced from the MPDB Database (JAHM Software Inc., USA). The primary data sources are as follows: thermal conductivity and specific heat capacity [49]; density was assumed to be 7,810 kg/m³ at room temperature [49]. As with the approach adopted by Malekipour et al. [48] the phase change was not accounted for in the model. A thermal model was used as described in the Abaqus manuals, with the build geometry and laser tool path replicating the experimental process.
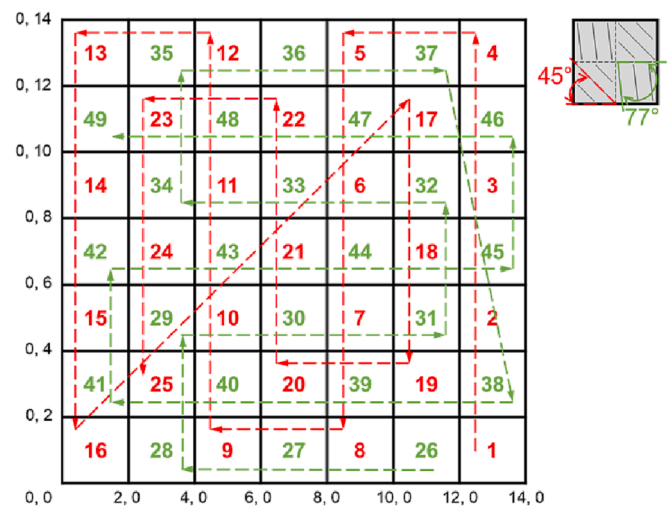

Fig. 3. The toolpath order of the chessboard strategy with coordinates in millimeters utilized in the finite element simulation. The numbers indicate the sequence of the squares being laser scanned. The laser track of a given layer is illustrated by the dashed line with arrow. Red color represents the squares scanned with laser track 45° from the edge of the build cube, while the green color is the laser track 77° away from the cube edge. (For interpretation of the references to color in this figure legend, the reader is referred to the web version of this article.)

Two thermal models were run with different time stepping:

(i) The maximum time step was limited to 0.3 ms to capture the detailed thermal history of the first layer of the build (at the laser speed of 950 mm/s, this time step ensures that the laser will only move ~ 0.285 mm per time increment);

(ii) A maximum time step of 50 ms to model the full part build. The starting temperature of the base plate was assumed to be 313 K. Heat exchange of the whole block (the build and the base plate) was calculated using a heat transfer coefficient of 18 W.m^{-2}.K^{-1} with a sink temperature of 313 K, and an emissivity coefficient of 0.25 [50] with an ambient temperature of 313 K. The laser power was defined as 280 W with an absorption coefficient of 0.5 and the double ellipsoid Goldak model used to define the heat flux input from the laser [50].

A tied contact was used between the built part and the substrate to reduce the required number of elements. 77,957 DC3D8 elements were used for the "high-resolution" heat transfer model of the first layer with an approximate global element size for the build part of 0.1 mm. For the full model, 80,309 elements were used with an approximate global element size for the build part of 0.5 mm.

2.7.2. Thermodynamic calculation

The thermodynamic analysis was conducted by FactSage 8.1 software package (GTT-Technologies, Germany). The Phase Diagram module was utilized for oxide phase prediction as a function of involved oxygen content in the liquid steel and processing temperature using equilibrium cooling calculation. The input data included the chemical composition of the steel powder and the oxygen contents in steel for the given condition. The database of FactPS, FToxid and FSstel were selected for calculation. The oxide phase solutions, slag liquid, monoxide, corundum, and spinel were selected. The liquid phase (Fe$_{liq}$), delta ferrite (bcc δ-Fe), austenite (fcc γ-Fe), and alpha ferrite (bcc α-Fe) were selected as steel solution candidates.

3. Results

3.1. Initial observation

The optical images of the etched 20MnCr5 steel samples by different scan strategies in both building direction (XZ plane) and transverse direction (XY) are presented in Fig. 4. The influence of the scan strategies is shown by the outline of the laser track and the as-solidified grain morphology. The sample produced by the linear scan strategy shows a uniform grain structure with the absence of the identical fish scale feature. Such morphological homogeneity is observed in both the XZ and XY planes (Fig. 4(a) and (c)). On the contrary, the sample fabricated using the chessboard strategy shows an obvious boundary of the melt pool, which is framed by the dark layers. To reveal the fine martensitic structure, please refer to the Fig. 7 in Section 3.2. The detailed microstructure in the melting pool of both linear and chessboard scan strategies has been presented using the electron microscopy technique for these micron to sub-micron sized features.

The surface characteristic of the L-PBF built 20MnCr5 samples with different scan strategies is shown in Fig. 5. The surface roughness was measured by the absolute depth of each individual position compared with the reference plane using the Alicona infinite focus microscope. A matrix of the depth value was generated with the sample position coordinates. Each height scattering curve is correlated to the position of a white dashed line in the corresponding image. The top view (XY plane) is presented in Fig. 5(a) and (c) for the linear strategy and Fig. 5(b) and (d) for the chessboard strategy, while the side view (XZ plane) is presented in Fig. 5(e) and (g) for the linear strategy and Fig. 5(f) and (h) for the chessboard strategy. The side surfaces (XZ plane) of the 20MnCr5 samples produced by the chessboard strategy represents a higher surface roughness, as the average surface roughness (Ra) of the linear strategy produced sample is 26 ± 3 μm, and Ra of the chessboard strategy produced sample is 30 ± 2 μm. The top surface (XY plane) of the sample produced using a chessboard strategy exhibits a higher roughness with Ra value of 22 ± 3 μm and the height fluctuation reaching ± 200 μm (Fig. 5(d)), while the linearly scanned sample shows an Ra value of $15 \pm$

2 μm and keeps a constant height scattering within ± 100 μm range (Fig. 5(c)). An interesting feature is also observed in Fig. 5(d), where the higher height scattering (curve peaks) is generally overlapped with the square boundaries (red dashed line). It is suggested that the boundaries of each square in the sample built with the chessboard strategy have formed a ridge surrounding the inner area of the given square (Fig. 5 (b)). The varying surface roughness in the two samples could be attributed to the scan strategy, as a significant change has been obtained in the top surface (XY plane) which is influenced by the laser scanning path.

The hardness variation of the samples by different scan strategies in both the XY and XZ planes, as a quantitative representation of the mechanical properties, is illustrated in Fig. 6. The hardness of the samples by the chessboard strategy is on average 323 ± 30 HV50 for the XZ plane and 330 ± 35 HV50 for the XY plane, lower than the samples produced by the linear strategy 368 ± 13 HV50 for the XZ plane and 367 ± 10 HV50 for the XY plane. The small standard deviation of the hardness observed in the linear build sample suggests a uniform microstructure. The more than doubled error bar of the sample produced by chessboard strategy seemingly indicates a heterogonous distribution of the microstructure and/or defects in the built 20MnCr5 sample.

The preliminary results indicate that the chessboard strategy has led the 20MnCr5 alloy to behave differently than the conventional linear approach, specifically in terms of the microstructure, surface roughness, and macro hardness. Therefore, it is important to understand the fundamental mechanism that triggered such phenomena from the aspects of microstructure evolution and bulk consolidation, using advanced characterization, thermal field analysis and thermodynamic calculations.

3.2. Microstructure evolution

The EBSD results in Fig. 7, taken from the XZ-plane, reveal the microstructural details of the melt pool in the 20MnCr5 samples. The build fabricated using the linear strategy formed a deeper melt pool (~65.2 μm, 6 layers in 391 μm, Fig. 7(a)) compared to the samples
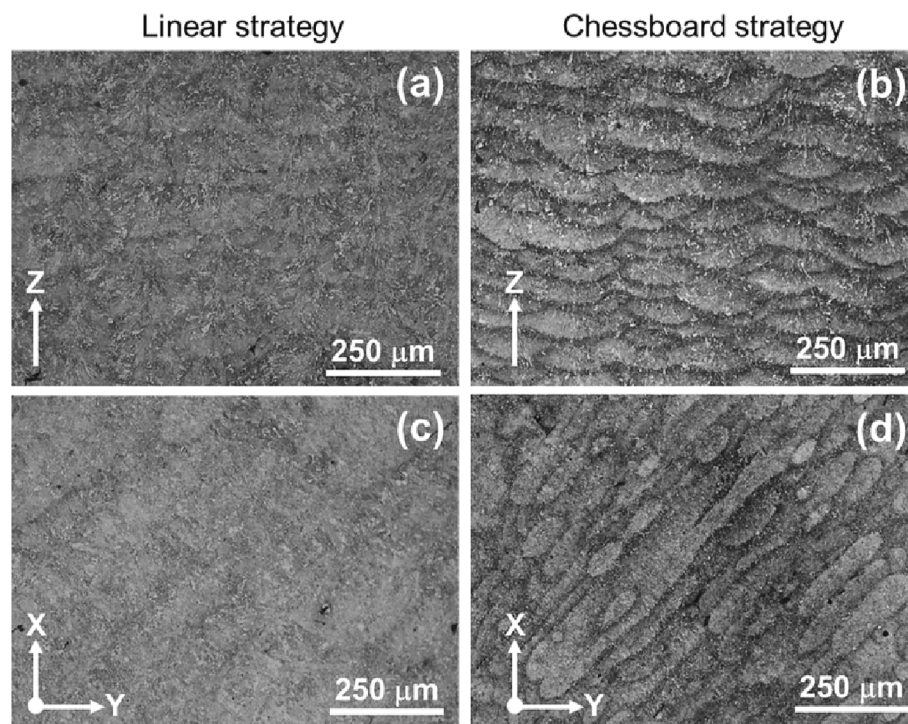

Fig. 4. The optical microstructure of the as-built 20MnCr5 steel, (a) and (c) produced with a linear scan strategy, and (b) and (d) produced with a chessboard scan strategy.
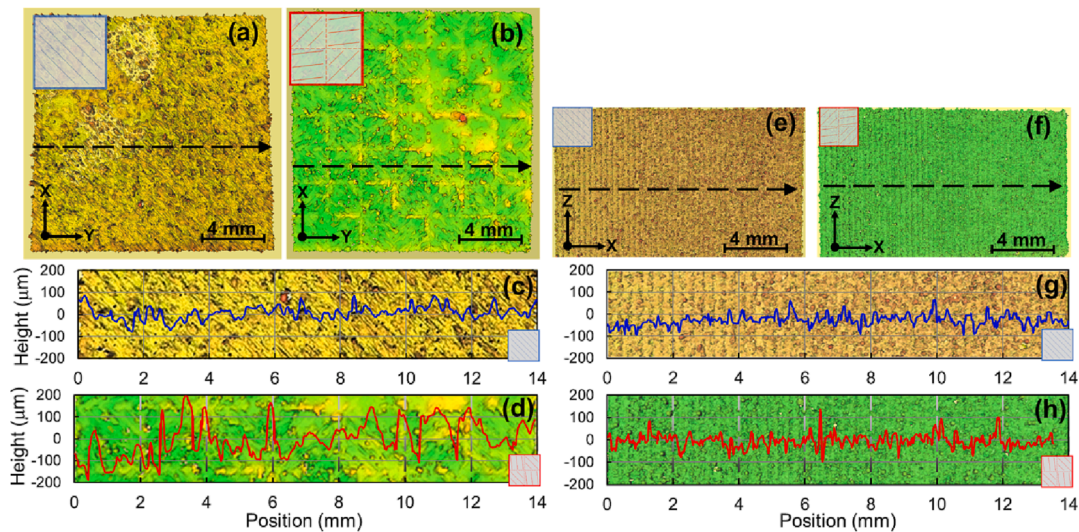
Fig. 5. The surface roughness (surface image and the corresponding topographic profile of the black arrow in the surface image) of the 20MnCr5 samples using the linear and chessboard scan strategies from top view and side view: (a) and (c) topographic image and the height profile of the sample with the linear strategy under top view, (b) and (d) topographic image and height profile of the sample with the chessboard strategy under top view, (e) and (g) topographic image and height profile of the sample with the linear strategy under side view, (f) and (h) topographic image and height profile of the sample with the chessboard strategy under side view.
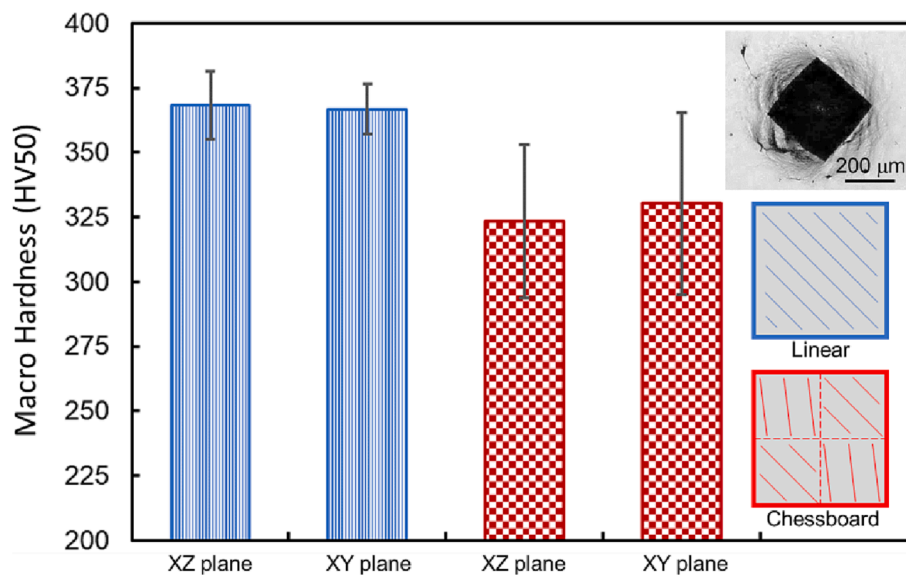

Fig. 6. The macro-Vickers hardness of the 20MnCr5 samples measured in the XY and XZ planes represents the collective response to the influence of the 20MnCr5 steel builds using linear and chessboard strategies.

fabricated using the chessboard strategy (~39.1 μm, 10 layers in 391 μm, Fig. 7(d)).

The low magnification inverse pole figures (IPFs) in Fig. 7(b) and (e) show a distinguishable morphological difference in the samples using linear and chessboard strategies. In the samples with the linear strategy (Fig. 7(b)), a columnar morphology is obtained with a deep melting pool. The shallow melting region in Fig. 7(e) suggests an equiaxed structure. A high magnification EBSD analysis is presented in Fig. 8. Additionally, the residual stress of the as-fabricated samples associated with solidification was measured using the Kernel Average Misorientation (KAM) method. This physical value describes the local misorientation between the orientation of a given pixel and its neighboring orientations with a defined kernel size and is commonly considered as a representation of the residual stress in the sample [51,52]. In this work, KAM values were extracted from the EBSD data by using the 2nd order

neighbors with a threshold angle of 5° [51]. The quantitative data from the KAM maps (Fig. 7(c) and (f)) resulted in an average KAM angle of 0.98° and 0.83° for linear and chessboard scan strategies, respectively. It indicates that the samples produced by both strategies retained a similar low residual stress, while the chessboard strategy further reduced the internal residual stress of the steel build.

Since the significant differences can be observed in Fig. 7 regarding the melt pool morphology and local residual stress in the building direction for the two laser scan conditions, a detailed microstructural study was conducted to investigate the effect of the scan strategy on martensite morphology and non-metallic inclusions. Fig. 8 shows the statistical analysis of the martensite structure of the 20MnCr5 build, including width and the aspect ratio of the martensite laths, as well as the detailed morphology. Clear differences in the development of the martensite phase are evident. Three clearly distinguishable martensite
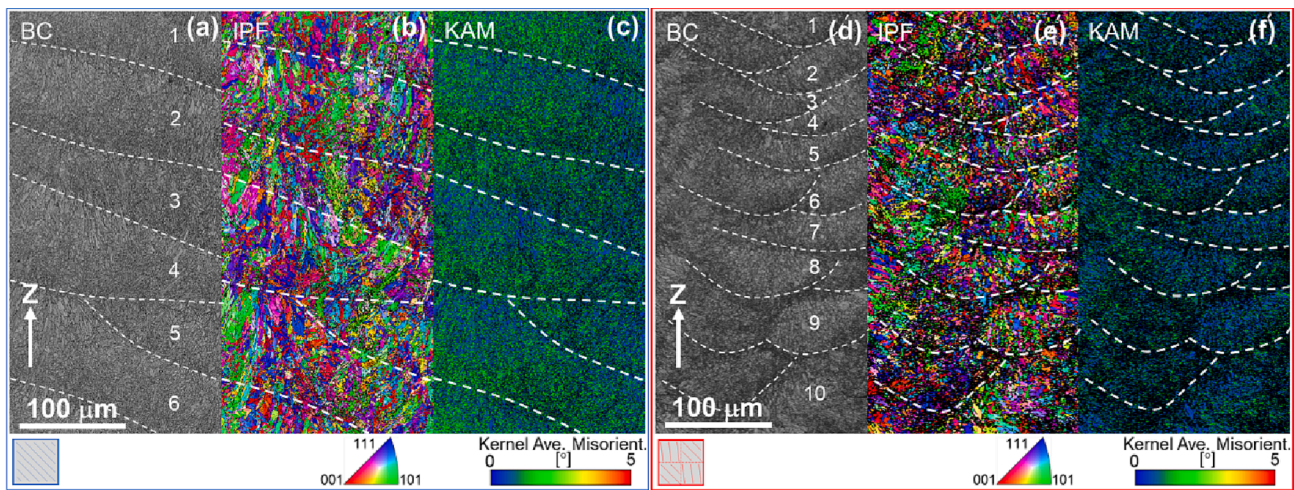
Fig. 7. The EBSD analysis of the 20MnCr5 samples with different scan strategies in the XZ-plane, (a)-(c) produced using the linear strategy, and (d)-(f) produced using the chessboard strategy. BC stands for Band Contrast image, IPF stands for Inverse Pole Figure, and KAM stands for Kernel Average Misorientation (KAM) map.
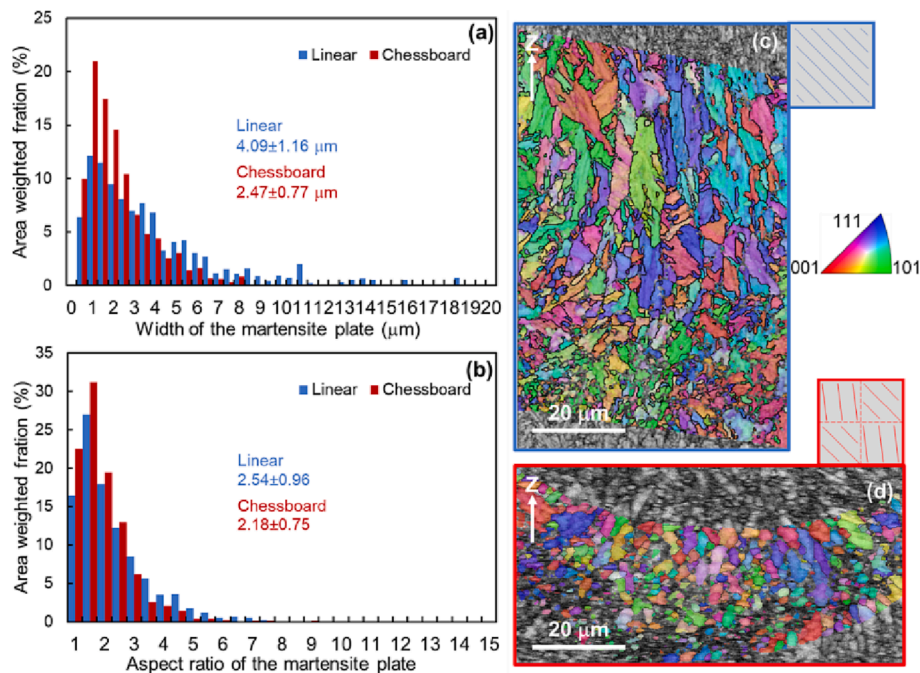

Fig. 8. The statistical analysis of the martensite structure and the detailed morphologies within the laser track (a) width of the martensite lath, (b) aspect ratio of the martensite lath, (c) and (d) the detailed martensite morphologies of samples produced by the linear and chessboard strategies, respectively.

lath features are observed in Fig. 8:

(i) In Fig. 8(a), the sample fabricated using the linear strategy presents a martensite lath width of 4.1 ± 1.2 μm, with a portion of the data spreading above 10 μm width. On the other hand, the sample produced using the chessboard strategy shows a narrow width of 2.5 ± 0.8 μm, with a concentration of values below 3 μm. The fitted minor diameter of the ellipse extracted from the Grain Detection function of the Aztec software was utilized to represent the width of martensite laths.

(ii) The aspect ratios (represented by the fitted ellipse aspect ratio) of the martensite lath (Fig. 8(b)) in the linear scan strategy and chessboard strategy cases are 2.5 ± 1.0, and 2.2 ± 0.8, respectively.

(iii) The coarse columnar martensite observed in Fig. 8(c) contributes to the higher lath width and larger martensite aspect ratio in the

sample fabricated using the linear scan strategy. On the contrary, the structure of the sample produced by the chessboard strategy (Fig. 8 (d)) maintains a uniform lath width with a low aspect ratio towards equiaxed morphology (aspect ratio equal to one).

According to the boundary strengthening mechanism, the refined martensite structure observed in the sample fabricated using the chessboard strategy is expected to provide higher mechanical performance [53].

Fig. 9 illustrates the orientation distribution function (ODF) maps obtained from the low magnification EBSD acquisitions of the samples produced by both scan strategies. In both cases, low texture intensity and random orientation of the martensite structure can be observed. The ODF sections show some identical orientations, but the overall intensities are below 3 MRD (Multiples of Random Distribution), indicating the random and low texture intensified microstructures in both
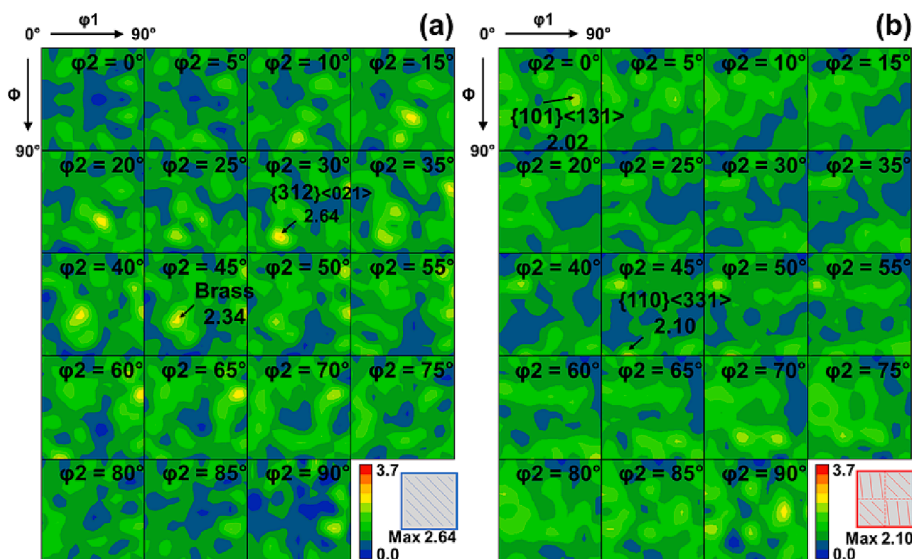
Fig. 9. The orientation distribution function (ODF) maps of the samples prepared with different scan strategies of (a) linear strategy, and (b) chessboard strategy.

linear and chessboard samples. This can be attributed to the refined structure of the parent austenite phase formed from the high temperature ferrite along the direction of decreasing temperature of the local melt pool. A reproducible orientation relationship between the parent (γ-Fe) and product (α-Fe) lattice is well recognized in the martensitic transformation as the Kurdjumov-Sachs relationship [54]. As a result, the orientation distribution of the parent austenite phase directly influenced the follow-on martensite texture. Compared to conventional continuous casting processes, the L-PBF offers a high cooling rate, leading to the microstructural refinement in various steel grades [7]. This refinement contributes to the random orientation distribution of the parent austenite structure.

The presence of non-metallic inclusions is a significant factor in determining the mechanical properties of low alloy steel [55]. Fig. 10 represents the statistical analysis of the two strategy cases based on 300 high magnification SEM-BSE images, covering a total region of 0.15 mm^2 from both the XY and XZ planes. The distribution of inclusion size is generally similar in the range below 0.2 μm. However, in the case of

the chessboard strategy sample, a slightly higher frequency is observed in the 0.025 to 0.05 μm range (insert in Fig. 10). In addition, an increased number of large inclusions can be observed in the sample produced by the chessboard strategy in Fig. 10 (dashed rectangle and inserted BSE image). These coarse inclusions can often have a detrimental effect on the fracture toughness and negatively impact ductility. However, they can potentially contribute to increased macro hardness as hard particles are capable of bearing increased loads in the indentation region, resulting in higher hardness values.

3.3. Consolidation performance

Porosity analysis was performed in Avizo 2021.2 on the extracted pore data from XCT scanning. Analysis of the pore data shows a large difference in pore diameter between the linear and chessboard printing strategies (Fig. 11). The sample produced by the linear strategy presented a porosity content of 0.39 vol%, compared to a porosity content of 1.23 vol% by the chessboard strategy. Pore sizes were also
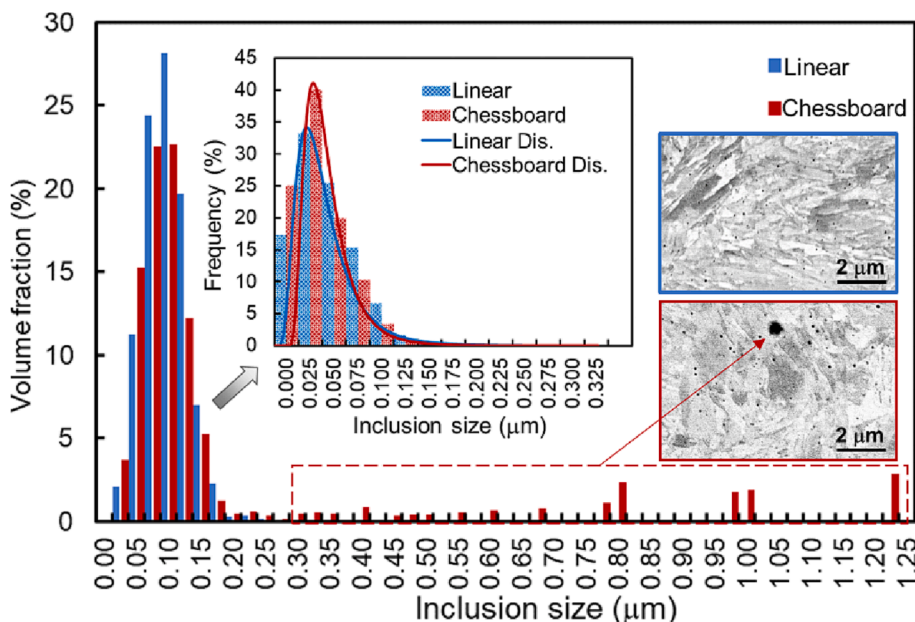
Fig. 10. The statistical analysis of the inclusion distribution of the 20MnCr5 samples fabricated by the linear and chessboard strategies. The average inclusion size is 0.055 ± 0.032 μm for the linear strategy case. In the sample made by the chessboard strategy, the average inclusion size is 0.047 ± 0.034 μm. The fine inclusions show a similar size distribution as the linear strategy counterpart, while larger sized inclusions can be seen in the BSE image (red dashed rectangle). (For interpretation of the references to color in this figure legend, the reader is referred to the web version of this article.)

Fig. 11. The porosity size distribution obtained by the XCT. The sample produced using the chessboard strategy shows a higher porosity and larger porosity size.

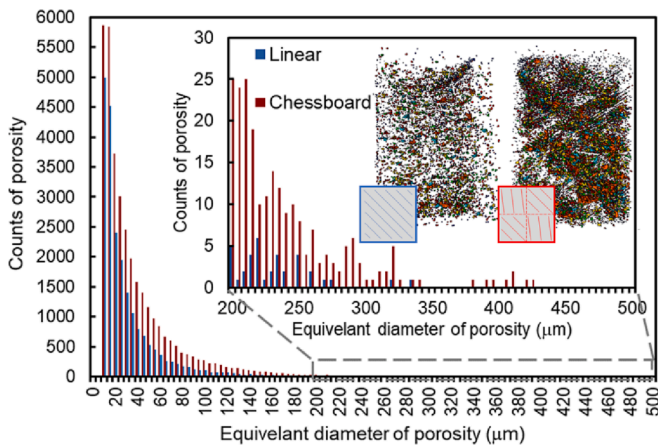consistently larger in the chessboard strategy, on an average of 78 ± 1 µm compared to 62 ± 1 µm in the linear strategy (95% confidence intervals). The lack of overlap between confidence intervals in both populations suggests that both scan strategies have a characteristic difference in pore sizes. Cohen's *d* calculated between pore lengths of both printing strategies gives a value of 0.199, reporting a small effect size.

Comparisons of pore volumes agreed with these results, with the mean pore volume being higher in the chessboard strategy (18.75 ± 1.08 × 10^4 µm^3) than in the linear printing strategy (0.87 ± 0.58 × 10^4 µm^3). Again, the lack of overlap between confidence intervals suggests a characteristic difference between the volumes of pores in both scan strategies. Cohen's *d* calculated between pore volumes of both printing strategies gives a value of 0.129, reporting a very small effect size.

Overall, it is observed that both pore size and volume are higher in the sample produced using the chessboard printing strategy compared to the linear printing strategy. This indicates that the chessboard strategy yields lower overall print quality in terms of the presence and size of pores within the build.

The as-fabricated samples were further analyzed using Archimedes' principle to measure the relative density, as shown in Fig. 12(a). The sample fabricated using the linear strategy exhibited a higher density of 97 ± 2% compared to the chessboard strategy, which had a density of 95 ± 2%. It is also worth noting that the powder feedstock used may have had a mild influence on the relative density of the samples produced by both linear and chessboard strategies. This is because the powder size distribution included a small portion of coarse particles (less than 150 µm), which is larger than the layer thickness of 40 µm. The presence of large particles could affect the powder-bed packing density [56]. It is

expected that the relative density obtained in this study could be increased using newly commercialized 20MnCr5 steel feedstock with a particle size range of 15–55 µm [57].

In addition, a low magnification microstructural study and quantitative porosity analysis were performed on the XZ plane of both samples, as shown in Fig. 12(b) and (c). The images were sliced along the Z direction with a width of 120 µm, resulting in a total of 85 slices being obtained. Each slice was analyzed, and the porosity data was collected to plot the curves of the porosity volume fraction. The sample fabricated using the chessboard strategy exhibits a periodical variation in the porosity volume fraction. The high peaks in Fig. 12(c) indicate a porosity volume fraction exceeding 7% and are separated by regions with low porosity. In contrast, the sample fabricated using the linear strategy presents a more consistent scattering of porosity levels, with values below 2%.

From both Figs. 11 and 12, it can be observed that samples produced by the chessboard strategy exhibit a higher level of porosity defects. This higher porosity content could potentially explain the lower macro hardness observed in Fig. 6, despite the favorable microstructure features of these samples. The heterogeneous distribution of porosity in the chessboard strategy in Fig. 12(c), results in a significant variation in local mechanical performance within the as-built sample. This variation contributes to the large error bars observed in the macro hardness from chessboard strategy samples (Fig. 6).

A comprehensive compositional analysis was conducted using SEM-EDS to investigate the composition of the surrounding areas of the porosity. The results revealed the presence of relatively large inclusions in close proximity to the pores. Further analysis confirmed that these inclusions are primarily composed of oxides. More detailed information and discussion regarding these findings is presented in Section 4.

In Fig. 13, the morphology of the porosity region in the sample produced by the chessboard strategy is depicted. Fig. 13(b), (c) and (d) present detailed images showcasing three distinct pore structures. In Fig. 13(b), the presence of oxide inclusions (indicated by white arrows) at the corners of the solidified melt pool can be observed, hindering the integration of the molten metal. Additionally, a thick layer of oxide (indicated by the yellow arrows), resulting from the oxidized steel powder, forms a seal around the pure metal, further impeding integration [31]. A similar feature can be observed in Fig. 13(c), with the steel powder exhibiting a metallic surface (yellow arrow). The third pore morphology, as shown in Fig. 13(d), displays a clean surface on the pore wall. The oxide inclusions are presented at the corners where the liquid metal integrates to minimize surface tension during the laser heating. However, the presence of the oxide inclusion reduces the wetting of liquid steel to the oxide, acting as an obstacle that inhibits the integration of molten steel powders into one single liquid pool, resulting in the formation of a cavity region [31].

To investigate the underlying mechanisms responsible for the notable disparity in the consolidation behavior of 20MnCr5 samples fabricated using the linear and chessboard scan strategies, finite element

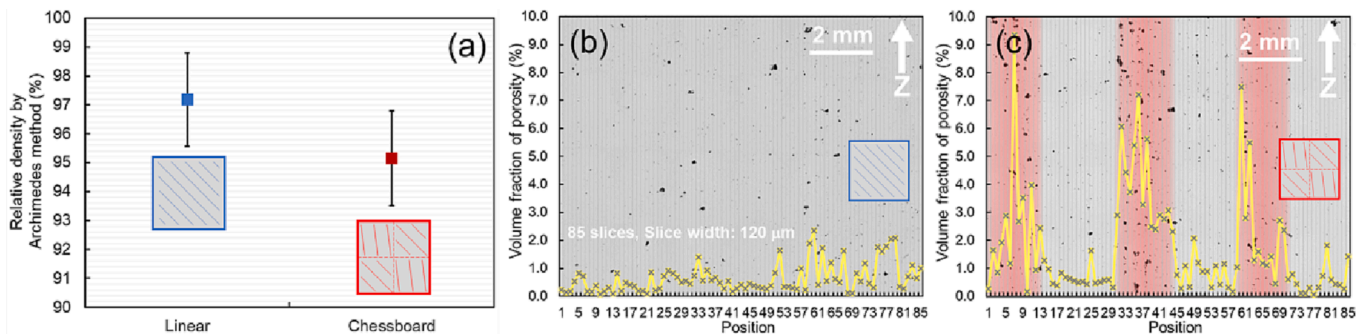
Fig. 12. The relative density of the as-built samples and the survey of the porosity distribution through the sample cross section, (a) relative density comparison using Archimedes' principle, (b) linear strategy, and (c) chessboard strategy.
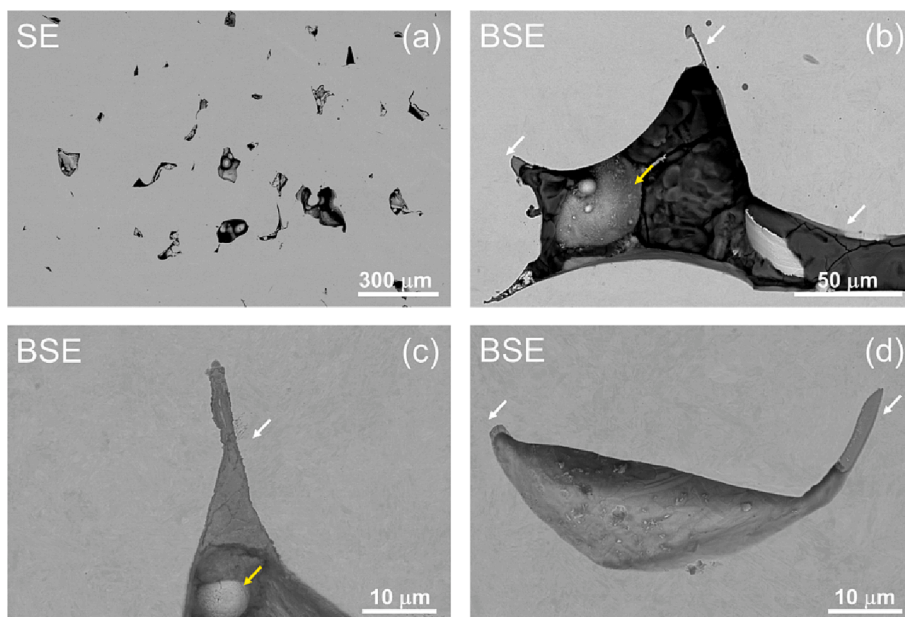
Fig. 13. The morphology of the porosity in the sample produced by chessboard scan strategy, (a) the porosity region, (b), (c), and (d) the typical morphology of the individual pores with the presence of oxide lumps (white arrows) and 20MnCr5 powder (yellow arrows if applicable). (For interpretation of the references to color in this figure legend, the reader is referred to the web version of this article.)

analysis and thermodynamic calculations were conducted to analyze the thermal field distribution and high-temperature reactions.

3.4. Thermal field variation

The laser power, scanning speed, and hatch distance are crucial parameters in the L-PBF process. In this study, these processing parameters were set constant to ensure the same input energy, while the scan strategy was varied. FEA simulation was conducted to analyze the temperature distribution on the XY plane after completing one layer scan, and the results are presented in Fig. 14. Fig. 14(a) shows the thermal gradient created by the linear scanning pattern, with a gradient from the scan start corner to the end position. On the other hand, Fig. 14 (b) depicts the high-temperature islands observed in the case of the chessboard scanning strategy. The temperature gradient in this case is from the scanning position within each chess square to its boundary, while the rest of the region remains relatively uniform. In Fig. 14(b), the white dashed line indicates the size of the chess squares, and the red

dashed line represents the maximum heating region within one chess square. The difference in surface topography observed in Fig. 5 can be attributed to the varying thermal field distributions resulting from the linear scanning and chessboard scanning strategies (Fig. 14). Enlightened by the simulation in Cheng et al.'s work [41], the geometry of the given scan pattern has a significant impact on the thermal profile in the L-PBF process. The inter-layer rotation angle, on the other hand, did not induce identical difference in the thermal profile of a given scan pattern during laser fusion. This suggests that the findings in the current research are applicable in the scenarios involving the rotation angle between the subsequent layers, as the scan patterns (linear and chessboard) are the primary factors influencing the thermal profile of the build.

Fig. 15 illustrates the temperature–time profiles for a specific coordinate (x, y) (9.0, 7.0) in both scanning strategies for 11 process cycles (layers). It should be noted that the thermal behavior observed at this coordinate is representative and similar to other coordinates in the build (see Fig. 3 for coordinate location). The cycles represent the laser
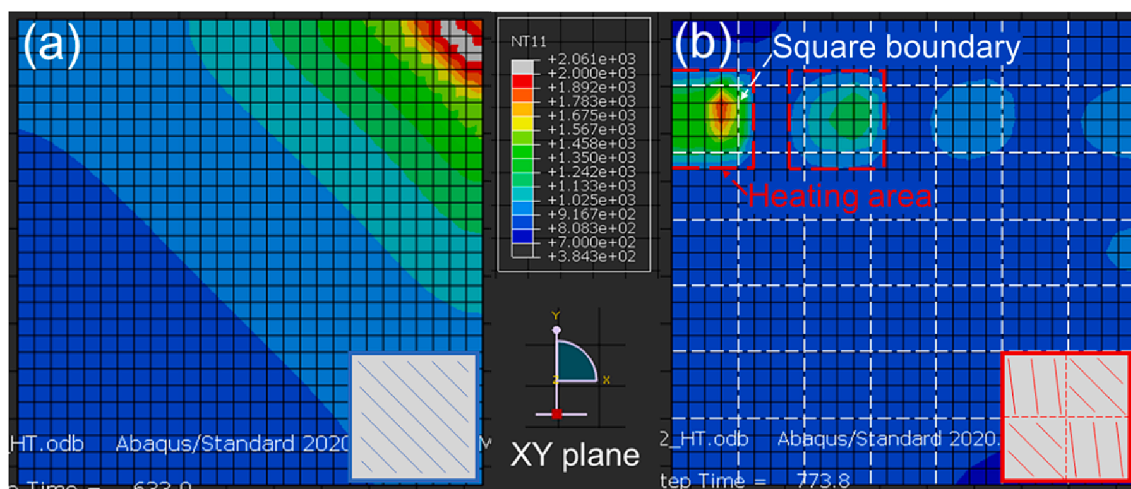

Fig. 14. Finite Element simulation of temperature on the XY plane, (a) linear and (b) chessboard scan strategies (legend indicates nodal temperature in degrees Kelvin).
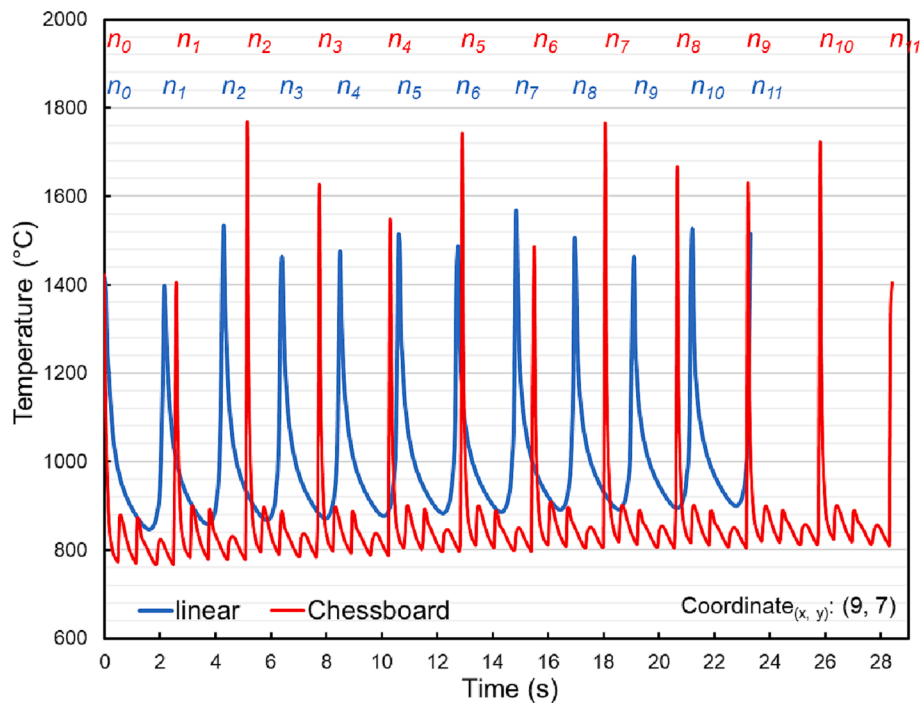
Fig. 15. The temperature history of a given position with coordinate(x,y) (9.0, 7.0) in the building process. The chessboard strategy takes a longer scanning time and higher melting temperature for each layer processed. The subsequent three minor temperature peaks in the chessboard strategy are due to the nearby chess squares been scanned.

heating process starting from the given coordinate position and ending when the laser returns to the same position. The time for each cycle is the same since it corresponds to the duration of one layer, with the only difference being the starting point. In the linear scanning strategy, the temperature curve exhibits a sharp peak followed by a gradual decrease. On the other hand, the chessboard scanning strategy shows a sharp peak indicating laser heating at the given position, which is also higher than the peak temperature observed in the linear scanning strategy. Following the initial peak, there are three minor peaks in close proximity, which could be influenced by the neighboring Squares 6, 7, 18, and 21, sharing the sides of same Square 44. A prolonged processing time can be observed in the case of the chessboard strategy, as in Fig. 15, the chessboard strategy only reached cycle 9 (n_9) when cycle 11 was completed in a linear pattern (n_{11}). The chessboard strategy requires 23.9% more time scanning each layer compared to the linear strategy. Such an extension in process time is caused by the scan repetition of the boundary line in between each pair of the neighboring squares. As volumetric energy density is the same for both scan patterns, the longer scanning time in the chessboard strategy leads to higher total energy input in an individual layer scanning process. Consequently, the heat accumulation in the sample processed using the chessboard strategy is higher.

In order to investigate the thermal influence at different positions during one layer processing, the temperature profiles of four selected positions in Square 44 were analyzed, as shown in Fig. 16(a). The blue curve represents the temperature profile at coordinate $_{(x, y)}$ (9.0, 7.0), which corresponds to the center of Square 44. The red curve corresponds to coordinate$_{(x, y)}$ (8.0, 6.0), which is the corner of Square 44 and is adjacent to Squares 7, 21, and 30. The green curve corresponds to position$_{(x, y)}$ (8.5, 6.5), which is halfway towards the corner, and the brown curve corresponds to position$_{(x, y)}$ (8.2, 6.2), which is a quarter away from the corner. Fig. 16(b) provides a visual representation of the neighboring squares of Square 44. Fig. 16(d), (e), and (f) show the enlarged temperature response of the given positions in Square 44 when the laser scans the neighboring Squares 7, 21, and 30. It can be observed that the corner position$_{(x, y)}$ (8.0, 6.0) experiences multiple heating

events, as indicated by the presence of four heating peaks in the temperature curves. On the other hand, the center of Square 44 experiences one major heating event when the laser processes Square 44. These thermal analyses indicate that the repetition of scanning along the boundaries of neighboring squares leads to heating overlap and accumulation of heat in the corner and boundary areas. In contrast, the center of a given square is relatively less affected. The repetitive heating of a localized area is not desirable in the L-PBF process, as it can interfere with the structural continuity and contribute to the formation of defects.

The combination of the periodical features observed in the porosity distribution (Fig. 12) and the thermal profile analysis showing an overlapped heating region (Fig. 16) suggests a strong connection between the overlapped heating region in the build using the chessboard strategy and the heterogeneous porosity distribution in the 20MnCr5 builds. This overlapped heating region is likely contributing to the large variation in Vickers hardness observed in samples fabricated using the chessboard scan strategy and is discussed in more detail in Section 4.

4. Discussion

To reveal the underlying mechanism for the porosity formation, thermodynamic calculation was utilized to understand the high-temperature reaction in the L-PBF process of the 20MnCr5 powder.

In the L-PBF process, the formation of pores is commonly attributed to factors such as insufficient laser power, excessively high scan speed [58], and gas entrapment [59]. These factors are typically considered from a processing standpoint. In this work, the presence of oxide inclusions in association with the pores (Fig. 13) indicates that the oxidation reaction and the deteriorated wetting characteristics of the liquid metal play a dominant role in the pore formation [32].

The thermodynamic calculation focused on predicting the oxide phase behaviour, as shown in Fig. 17(a). It indicates that the slag phase (SiO_2(liq)) occurs above 1500 °C with a low oxygen content in the liquid steel. The high-temperature δ-ferrous phase forms prior to the oxide species. This oxide phase then transforms into a solid quartz phase (SiO_2). The presence of the slag liquid inhibits the integration of
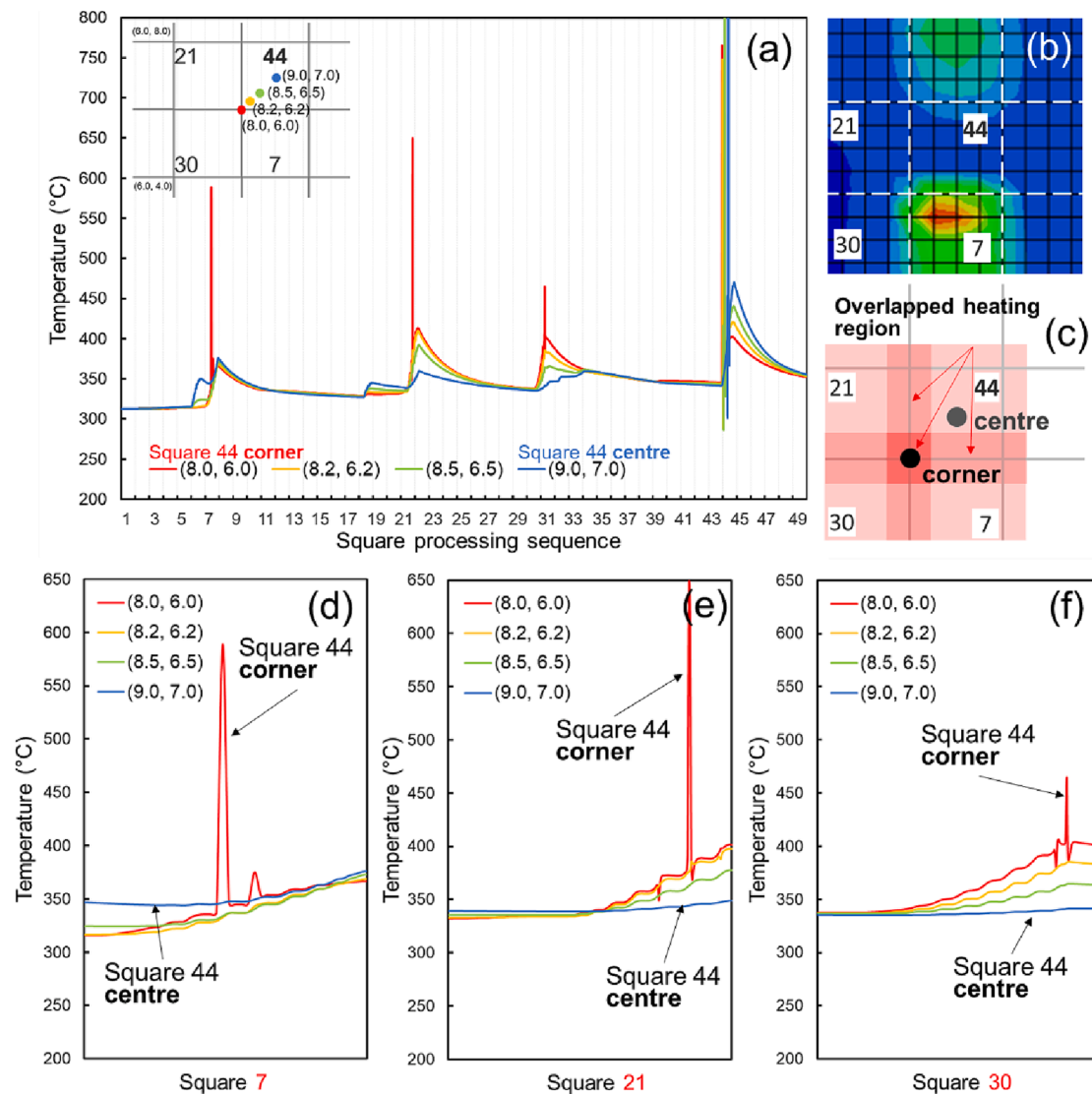
Fig. 16. The simulated thermal profile of the chessboard strategy in a layer building suggested an overlapping of laser process in the square edges and corners shared with neighboring squares, Square 44 is selected, where Squares 7, 21, and 30 are the neighborhood, (a) temperature curves of the given positions in Square 44 (center of square, corner of square) for the whole layer building, (b) the temperature map when processing Square 7 (white dashed line is the boundaries of each squares in the chessboard), (c) schematic illustration of the overlapped heating region in the square edges and corners when heating the neighboring squares, (d), (e), and (f) the detailed temperature curves of the given positions in Square 44 when process the neighboring Squares 7, 21, and 30, respectively.

δ-ferrous, which then transforms into solid silicon oxide in the position where the pores formed during the solidification of 20MnCr5 steel. In comparison, the liquid steel normally holds less than 10 ppm oxygen after ladle treatment in conventional steelmaking [60]. This value maintains in the continuous casting process, where the liquid steel is solidified into the billet with the given dimensional profile. Although the oxide phases still precipitate in the conventional steelmaking process (Fig. 17(a)), the influence of these oxides are minimized due to their trace quantities. The detailed EDS survey (Fig. 17(b)) has examined the oxide phase in a typical region where the oxide is located in between the solid metal and a pore. The highlighted silicon and oxygen signal in the EDS mapping from both the top view and cross-section planes confirmed that the lump oxide is silicon oxide. Considering the non-equilibrium nature of the laser fusion, this solid SiO_2 phase would be an amorphous silica by considering the results of selected area diffraction patterns using TEM characterization in our previous study [32].

The studies on the thermal oxidation of liquid/solid phases [61,62] indicate that the formation of oxides initially follows a linear growth rate, which is then followed by a parabolic growth rate as the process

continues over long durations, typically in the order of hours. In a short-duration oxidation study of a low alloy steel [63], it was observed that the linear growth rate of the oxidation product dominates the first several seconds of the oxidation process. This is close to the time scale of the laser scanning duration for each layer in both the linear and chessboard scan strategies, which is approximately 2 s (as shown in Fig. 15). The linear relationship of the oxidation reaction kinetics during the isothermal holding period is written as [61,63]:

$$W = K_l t \qquad (2)$$

where W is the mass gain of the oxide in g/mm^2, K_l is the linear oxidation rate constant at a given temperature T, and t is the oxidation time. The linear oxidation rate (K_l) is proportional to the holding temperature. According to Equation (2) and the temperature profiles in Fig. 15, the higher peak temperature (higher silicon diffusion rate) and the extended laser scan duration (longer reaction period) of the chessboard strategy are promoting the slag liquid (SiO_2(liq)) phase formation, and later silicon oxide lumps retained in the porosity region. As a consequence, the samples built with the chessboard strategy presented a higher
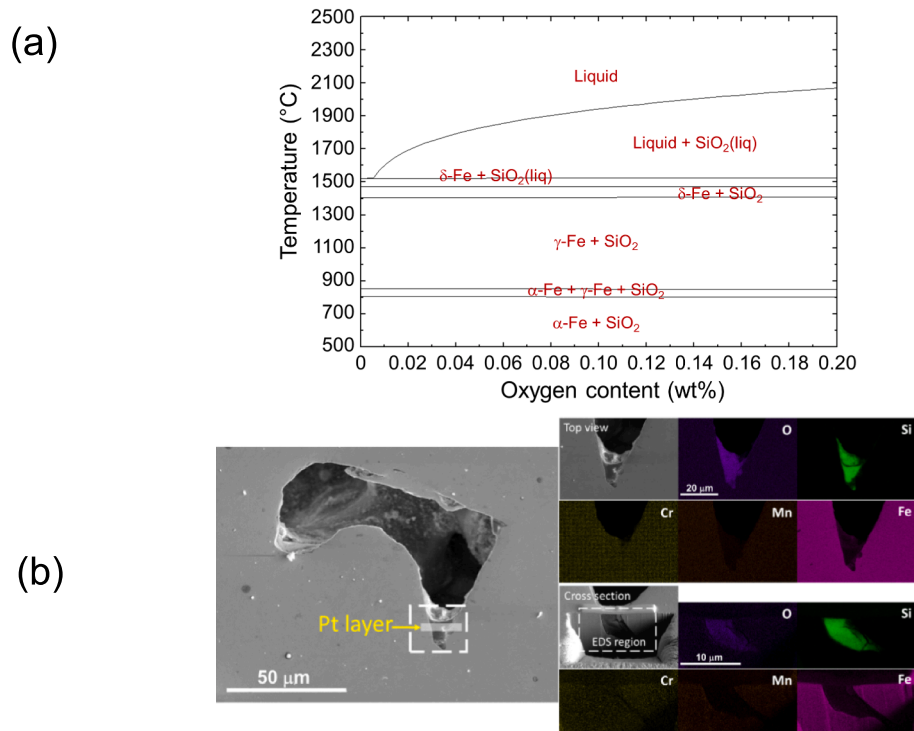
Fig. 17. Thermodynamic calculation of the relationship between the phase selection and the oxygen content in the liquid steel for the oxide phase prediction (a), and the confirmation by the FIB-EDS analysis for the chemical composition of the examined regions (top view and cross section) in chessboard sample (b).

porosity level and lower relative density compared to the samples produced by the linear scan strategy. The heterogeneous distribution of the porosity in the sample produced by the chessboard strategy could also be explained by the extended reaction time by the heating overlap in the square edges and corners illustrated in Fig. 16, which led to the specific topographic ridges in Fig. 5(a) and (d) and higher porosity regions in Fig. 12 (c). It is worth noting that spatter particles [64], which are highly oxidized, can also be incorporated into the next layer during the printing process. These particles can contribute to the formation of oxide and reduce the wetting of the liquid steel to the oxide layer and prevent the integration of the melt pool.

The observed reduction in mechanical performance in the 20MnCr5 sample produced using the chessboard strategy, as opposed to the reported benefits in other studies with stainless steel [21,65] can be attributed to the deteriorated metallurgical quality resulting from several factors:

(i) Large temperature region for slag liquid formation: the temperature region for the formation of slag liquid during the reaction of O_2 and Si atoms in liquid steel is approximately 500 K in the current study (Fig. 17(a)). In comparison, while the temperature region for $MnO \cdot Cr_2O_3$ dominated slag liquid in the Fe-18Cr-10Ni melt was less than 150 K [32].

(ii) Higher resistance to liquid steel integration: The higher presence of non-metallic inclusion, such as silicon oxide, in the current study affects the wetting behavior of the liquid steel. The wetting angle of liquid steel on the silicon oxide is higher than that on chromite [66]. As a result, higher energy is required to overcome the surface tension of SiO_2-Fe(liq) during solidification and thereby led to the formation of the pores.

In Section 3.1, both the martensite morphology and inclusion volume fraction of the sample by the chessboard strategy favour a higher hardness than the linear strategy. However, the overall hardness performance (Fig. 6) of the chessboard sample is 11.5% lower than the

sample processed by the linear strategy. It suggests that the poor consolidation behaviour in the form of high porosity is the underlying cause that significantly deteriorates the mechanical performance of the sample produced by the chessboard strategy. Such influence of the poor consolidation results from the *in-situ* formed oxide inclusions and deteriorated integration of the liquid steel. The chessboard strategy induced an excessive thermal profile to the building layer, which promoted oxidation in the laser-powder interaction.

The comparison study of the scan strategies in the L-PBF process of this low alloy 20MnCr5 steel has provided a new insight into the importance of considering non-metallic phase formation during powder fusion based AM. This study highlights the impact of high-temperature reactions and the presence of oxygen on the metallurgical quality of the build. The findings suggest that when dealing with oxidation-sensitive metals, such as 20MnCr5 steel, it is crucial to carefully optimize the processing parameters, including the laser scan strategies, to control the build's metallurgical quality. Inappropriate processing parameters can lead to deviations in the solidification route and inclusion metallurgy due to the formation of non-metallic phases through high-temperature reactions. To address these challenges and improve the overall quality of the as-built sample, several strategies can be considered. One approach is to optimize the unit energy input during the process, ensuring that the energy is distributed appropriately to minimize oxidation and non-metallic phase formation. Additionally, controlling the oxygen content in the processing atmosphere can help mitigate the detrimental effects on the metallurgical quality. By optimizing the unit energy input and/or eliminating the oxygen in the processing atmosphere, the defect level the as-built sample could be controlled and a higher mechanical performance to be expected in these metals by the advantage of the microstructure refinement using the chessboard strategy.

5. Conclusions

The low alloy 20MnCr5 steel, as an example of an oxidation sensitive

metal, while a low cost and robust material holding distinct metallurgical characteristics than those of the prestigious stainless steel or Ni superalloys, was subjected to the L-PBF process using both linear and chessboard scan strategies to understand its unique response to the processing parameter of scan strategies. This study aimed to investigate the material's unique response to different scan strategies by examining its microstructure evolution and consolidation behaviour through experimental analysis and theoretical simulations. The following points can be concluded from this work:

1. The linear scan strategy improves surface quality of the 20MnCr5 build (specifically in the XY plane) and increases hardness by approximately 11.5%, compared with the chessboard scan strategy.
2. Based on the Kernel Average Misorientation (KAM) measurement and the Orientation Distribution Function (ODF) analysis, low residual stress and low texture intensification were shown in the as-build samples by both linear and chessboard scan strategies.
3. The samples produced by the chessboard scan strategy obtained refined martensite laths (2.5 ± 0.8 μm and the aspect ratio of martensite laths of 2.2 ± 0.8) compared to the linear scan strategy (4.1 ± 1.2 μm with a portion of the data spread above 10 μm for lath width, and aspect ratio of 2.5 ± 1.0).
4. The sample produced by the chessboard strategy also shows a higher volume fraction of the non-metallic inclusion particles. Both the refined martensite structure and the high quantity of inclusion particles in the chessboard strategy samples did not benefit the hardness of the build due to the existence of defects in the build.
5. The sample produced by the chessboard strategy presents a higher level of porosity defects, which leads to a relative density of 95 ± 2%, while it is 97 ± 2% in the linear strategy. Heterogeneous and periodical distribution of porosity is also observed in the chessboard scan samples.
6. The FE analysis and the thermodynamic calculation suggest that the excessive temperature profile provided by the chessboard scan strategy and the residual oxygen presented in the processing chamber promoted the high-temperature reaction between the high-affinity element (here Si) and the oxygen. As a consequence, the *in-situ* formed silicon oxide inclusions prevented the integration of liquid steel and led to a high level of porosity in the build by the chessboard scan strategy.
7. For oxidation-sensitive metals, optimizing the unit energy input and/or eliminating the presence of oxygen could significantly reduce the porosity of the build and achieve higher mechanical performance by the advantage of the microstructure refinement using the chessboard scan strategy.

Declaration of Competing Interest

The authors declare that they have no known competing financial interests or personal relationships that could have appeared to influence the work reported in this paper.

Data availability

Data will be made available on request.

Acknowledgments

References

[1] W.E. Frazier, Metal additive manufacturing: a review, J. Mater. Eng. Perform. 23 (6) (2014) 1917–1928.
[2] W.J. Sames, F.A. List, S. Pannala, R.R. Dehoff, S.S. Babu, The metallurgy and processing science of metal additive manufacturing, Int. Mater. Rev. 61 (5) (2016) 315–360.
[3] H.R. Kotadia, G. Gibbons, A. Das, P.D. Howes, A review of Laser Powder Bed Fusion Additive Manufacturing of aluminium alloys: Microstructure and properties, Addit. Manuf. 46 (2021) 102155.
[4] T.D. Ngo, A. Kashani, G. Imbalzano, K.T. Nguyen, D. Hui, Additive manufacturing (3D printing): A review of materials, methods, applications and challenges, Compos. B Eng. 143 (2018) 172–196.
[5] B. Dutta, F.H. Froes, The Additive Manufacturing (AM) of titanium alloys, Met. Powder Rep. 72 (2) (2017) 96–106.
[6] K.N. Amato, S.M. Gaytan, L.E. Murr, E. Martinez, P.W. Shindo, J. Hernandez, S. Collins, F. Medina, Microstructures and mechanical behavior of Inconel 718 fabricated by selective laser melting, Acta Mater. 60 (5) (2012) 2229–2239.
[7] P. Bajaj, A. Hariharan, A. Kini, P. Kürnsteiner, D. Raabe, E.A. Jägle, Steels in additive manufacturing: A review of their microstructure and properties, Mater. Sci. Eng. A 772 (2020) 138633.
[8] L. Thijs, K. Kempen, J.-P. Kruth, J. Van Humbeeck, Fine-structured aluminium products with controllable texture by selective laser melting of pre-alloyed AlSi10Mg powder, Acta Mater. 61 (5) (2013) 1809–1819.
[9] L.E. Murr, S.M. Gaytan, D.A. Ramirez, E. Martinez, J. Hernandez, K.N. Amato, P.W. Shindo, F.R. Medina, R.B. Wicker, Metal fabrication by additive manufacturing using laser and electron beam melting technologies, J. Mater. Sci. Technol. 28 (1) (2012) 1–14.
[10] K. Kempen, L. Thijs, J. Van Humbeeck, J. Kruth, Processing AlSi10Mg by selective laser melting: parameter optimisation and material characterisation, Mater. Sci. Eng. 31 (2015) 917–923.
[11] A. Yadollahi, N. Shamsaei, Additive manufacturing of fatigue resistant materials: Challenges and opportunities, Int. J. Fatigue 98 (2017) 14–31.
[12] D. Kong, C. Dong, X. Ni, X. Li, Corrosion of metallic materials fabricated by selective laser melting, npj Mater. Degrad. 3 (2019) 1–14.
[13] M. Simonelli, Y.Y. Tse, C. Tuck, Effect of the build orientation on the mechanical properties and fracture modes of SLM Ti–6Al–4V, Mater. Sci. Eng. A 616 (2014) 1–11.
[14] S. Das, Physical aspects of process control in selective laser sintering of metals, Adv. Eng. Mater. 5 (10) (2003) 701–711.
[15] A. Durga, N.H. Pettersson, S.B.A. Malladi, Z. Chen, S. Guo, L. Nyborg, G. Lindwall, Grain refinement in additively manufactured ferritic stainless steel by in situ inoculation using pre-alloyed powder, Scr. Mater. 194 (2021) 113690.
[16] S.Y. Zhou, Y. Su, H. Wang, J. Enz, T. Ebel, M. Yan, Selective laser melting additive manufacturing of 7xxx series Al-Zn-Mg-Cu alloy: Cracking elimination by co-incorporation of Si and TiB2, Addit. Manuf. 36 (2020) 101458.
[17] K. Schmidtke, F. Palm, A. Hawkins, C. Emmelmann, Process and mechanical properties: applicability of a scandium modified Al-alloy for laser additive manufacturing, Phys. Procedia 12 (2011) 369–374.
[18] Q. Tan, Y.u. Yin, Z. Fan, J. Zhang, Y. Liu, M.-X. Zhang, Uncovering the roles of LaB6-nanoparticle inoculant in the AlSi10Mg alloy fabricated via selective laser melting, Mater. Sci. Eng. A 800 (2021) 140365.
[19] Q. Tan, Y.u. Yin, A. Prasad, G. Li, Q. Zhu, D.H. StJohn, M.-X. Zhang, Demonstrating the roles of solute and nucleant in grain refinement of additively manufactured aluminium alloys, Addit. Manuf. 49 (2022) 102516.
[20] D. Zhang, A. Prasad, M.J. Bermingham, C.J. Todaro, M.J. Benoit, M.N. Patel, D. Qiu, D.H. StJohn, M.a. Qian, M.A. Easton, Grain refinement of alloys in fusion-based additive manufacturing processes, Metall. Mater. Trans. A 51 (9) (2020) 4341–4359.
[21] X. Zhang, H. Xu, Z. Li, A. Dong, D. Du, L. Lei, G. Zhang, D. Wang, G. Zhu, B. Sun, Effect of the scanning strategy on microstructure and mechanical anisotropy of Hastelloy X superalloy produced by Laser Powder Bed Fusion, Mater Charact 173 (2021) 110951.
[22] F. Geiger, K. Kunze, T. Etter, Tailoring the texture of IN738LC processed by selective laser melting (SLM) by specific scanning strategies, Mater. Sci. Eng. A 661 (2016) 240–246.
[23] N. Nadammal, S. Cabeza, T. Mishurova, T. Thiede, A. Kromm, C. Seyfert, L. Farahbod, C. Haberland, J.A. Schneider, P.D. Portella, G. Bruno, Effect of hatch length on the development of microstructure, texture and residual stresses in selective laser melted superalloy Inconel 718, Mater. Des. 134 (2017) 139–150.
[24] J.J. Marattukalam, D. Karlsson, V. Pacheco, P. Beran, U. Wiklund, U. Jansson, B. Hjörvarsson, M. Sahlberg, The effect of laser scanning strategies on texture, mechanical properties, and site-specific grain orientation in selective laser melted 316L SS, Mater. Des. 193 (2020) 108852.
[25] M.P. Haines, F. List, K. Carver, D.N. Leonard, A. Plotkowski, C.M. Fancher, R.R. Dehoff, S.S. Babu, Role of scan strategies and heat treatment on grain structure evolution in Fe-Si soft magnetic alloys made by laser-powder bed fusion, Addit. Manuf. 50 (2022) 102578.
[26] P. Kontis, E. Chauvet, Z. Peng, J. He, A.K. da Silva, D. Raabe, C. Tassin, J.-J. Blandin, S. Abed, R. Dendievel, B. Gault, G. Martin, Atomic-scale grain boundary engineering to overcome hot-cracking in additively-manufactured superalloys, Acta Mater. 177 (2019) 209–221.
[27] L. Robatto, R. Rego, J. Mascheroni, A. Kretzer, I. Criscuolo, A. Borille, Evolution of Residual Stresses induced by different L-PBF build orientations along a post-processing chain of 20MnCr5 steel, Procedia CIRP 108 (2022) 873–878.

[28] X. Cui, S. Zhang, C.H. Zhang, J. Chen, J.B. Zhang, S.Y. Dong, A comparison on microstructure features of 24CrNiMo low alloy steel prepared by selective laser melting and laser melting deposition, Vacuum 191 (2021) 110394.

[29] T. Fedina, J. Sundqvist, J. Powell, A.F.H. Kaplan, A comparative study of water and gas atomized low alloy steel powders for additive manufacturing, Addit. Manuf. 36 (2020) 101675.

[30] Zadi-Maad A, Rohib R, Irawan A. Additive manufacturing for steels: A review. IOP Conference Series: Mater. Sci. Eng. 2018;285:012028.

[31] X. Yang, F. Gao, F. Tang, X. Hao, Z. Li, Effect of Surface Oxides on the Melting and Solidification of 316L Stainless Steel Powder for Additive Manufacturing, Metall. Mater. Trans. A 52 (10) (2021) 4518–4532.

[32] X. Yang, F. Tang, X. Hao, Z. Li, Oxide Evolution During the Solidification of 316L Stainless Steel from Additive Manufacturing Powders with Different Oxygen Contents, Metall. Mater. Trans. B 52 (4) (2021) 2253–2262.

[33] M. Song, X. Lin, F. Liu, H. Yang, W. Huang, Effect of environmental oxygen content on the oxide inclusion in laser solid formed aisi 420 stainless steel, Mater. Des. 90 (2016) 459–467.

[34] D. Eo, S. Park, J. Cho, Inclusion evolution in additive manufactured 316L stainless steel by laser metal deposition process, Mater. Des. 155 (2018) 212–219.

[35] P.u. Deng, M. Karadge, R.B. Rebak, V.K. Gupta, B.C. Prorok, X. Lou, The origin and formation of oxygen inclusions in austenitic stainless steels manufactured by laser powder bed fusion, Addit. Manuf. 35 (2020) 101334.

[36] D.I.N. En, 10084:2008–06., Case hardening steels - Technical delivery conditions, German version EN 10084 (2008) (2008) 2022.

[37] EOS. Technical Description EOSINT M 280. 2011;2022.

[38] U.S. Bertoli, A.J. Wolfer, M.J. Matthews, J.R. Delplanque, J.M. Schoenung, On the limitations of volumetric energy density as a design parameter for selective laser melting, Mater. Des. 113 (2017) 331–340.

[39] W. Hearn, R. Steinlechner, E. Hryha, Laser-based powder bed fusion of non-weldable low-alloy steels, Powder Metall. 65 (2) (2022) 121–132.

[40] L. Parry, I.A. Ashcroft, R.D. Wildman, Understanding the effect of laser scan strategy on residual stress in selective laser melting through thermo-mechanical simulation, Addit. Manuf. 12 (2016) 1–15.

[41] B. Cheng, S. Shrestha, K. Chou, Stress and deformation evaluations of scanning strategy effect in selective laser melting, Addit. Manuf. 12 (2016) 240–251.

[42] H. Jia, H. Sun, H. Wang, Y.i. Wu, H. Wang, Scanning strategy in selective laser melting (SLM): a review, Int. J. Adv. Manuf. Technol. 113 (9-10) (2021) 2413–2435.

[43] M. Strantza, R.K. Ganeriwala, B. Clausen, T.Q. Phan, L.E. Levine, D.C. Pagan, J.P. C. Ruff, W.E. King, N.S. Johnson, R.M. Martinez, V. Anghel, G. Rafailov, D. W. Brown, Effect of the scanning strategy on the formation of residual stresses in additively manufactured Ti-6Al-4V, Addit. Manuf. 45 (2021) 102003.

[44] E. Ramirez-Cedillo, M.J. Uddin, J.A. Sandoval-Robles, R.A. Mirshams, L. Ruiz-Huerta, C.A. Rodriguez, H.R. Siller, Process planning of L-PBF of AISI 316L for improving surface quality and relating part integrity with microstructural characteristics, Surf. Coat. Technol. 396 (2020) 125956.

[45] ASTM International. ASTM B962-17 Standard Test Methods for Density of Compacted or Sintered Powder Metallurgy (PM) Products Using Archimedes' Principle. 2017.

[46] Crozet D, Mogire E. Metallographic preparation of Fasteners Microscopic assessment and analysis. 2020;2022.

[47] ASTM. Standard Test Methods for Vickers Hardness and Knoop Hardness of Metallic Materials. 2017.

[48] E. Malekipour, H. El-Mounayri, M. Marrey, E.J. Faierson, M.A. Hasan, An innovative Fast Layer-wise Simulation of Temperature distribution using a Chessboard Strategy (FALS TECHS) in the powder-bed fusion process, Addit. Manuf. 46 (2021) 102065.

[49] ASM International, Handbook Committee. ASM handbook Volume 1: Properties and Selection: Irons, Steels, and High-performance Alloys. : ASM, International (1990).

[50] X.u. Song, S. Feih, W. Zhai, C.-N. Sun, F. Li, R. Maiti, J. Wei, Y. Yang, V. Oancea, L. Romano Brandt, A.M. Korsunsky, Advances in additive manufacturing process simulation: Residual stresses and distortion predictions in complex metallic components, Mater. Des. 193 (2020) 108779.

[51] L.N. Brewer, D.P. Field, C.C. Merriman, Mapping and assessing plastic deformation using EBSD, in: A.J. Schwartz, M. Kumar, B.L. Adams, D.P. Field (Eds.), Electron Backscatter Diffraction in Materials Science, Springer US, Boston, MA, 2009, pp. 251–262.

[52] Y. Zhang, T. Yu, R. Xu, J. Thorborg, W. Liu, J. Tischler, A. Godfrey, D. Juul Jensen, Local residual stresses and microstructure within recrystallizing grains in iron, Mater Charact 191 (2022) 112113.

[53] A. Bag, K.K. Ray, E.S. Dwarakadasa, Influence of martensite content and morphology on tensile and impact properties of high-martensite dual-phase steels, Metall. Mater. Trans. A 30 (5) (1999) 1193–1202.

[54] G. Kurdjumov, G. Sachs, Over the mechanisms of steel hardening, Z.Phys 64 (1930).

[55] P.A. Thornton, The influence of nonmetallic inclusions on the mechanical properties of steel: A review, J. Mater. Sci. 6 (4) (1971) 347–356.

[56] Elliott AM, Nandwana P, Siddel D, Compton BG. A method for measuring powder bed density in binder jet additive manufacturing process and the powder feedstock characteristics influencing the powder bed density. 2016.

[57] EOS. Case hardening steel for 3D printing 20MnCr5. https://www.eos.info/en/3d-printing-materials/metals/case-hardening-steel.

[58] D. Gu, Y. Shen, Balling phenomena in direct laser sintering of stainless steel powder: Metallurgical mechanisms and control methods, Mater. Des. 30 (8) (2009) 2903–2910.

[59] M. Bayat, A. Thanki, S. Mohanty, A. Witvrouw, S. Yang, J. Thorborg, N.S. Tiedje, J. H. Hattel, Keyhole-induced porosities in Laser-based Powder Bed Fusion (L-PBF) of Ti6Al4V: High-fidelity modelling and experimental validation, Addit. Manuf. 30 (2019) 100835.

[60] G.G. Mikhailov, L.A. Chernova, Thermodynamic analysis of steel deoxidation with calcium and aluminum, Russian Metallurgy (Metally) 2008 (8) (2008) 727–729.

[61] N. Sano, Y. Matsushita, Kinetics of Silicon Oxidation from Liquid Iron Droplets, Trans. Iron Steel Instit. Japan 11 (4) (1971) 232–239.

[62] Ng KK, Polito WJ, Ligenza JR. Growth kinetics of thin silicon dioxide in a controlled ambient oxidation system. Appl. Phys. Lett. 1984, 44, 626-8.

[63] R.Y. Chen, W. Yuen, Short-time oxidation behavior of low-carbon, low-silicon steel in air at 850–1,180 C—I: oxidation kinetics, Oxid. Met. 70 (2008) 39–68.

[64] M. Yakout, I. Phillips, M.A. Elbestawi, Q. Fang, In-situ monitoring and detection of spatter agglomeration and delamination during laser-based powder bed fusion of Invar 36, Opt. Laser Technol. 136 (2021) 106741.

[65] P. Bian, J. Shi, Y. Liu, Y. Xie, Influence of laser power and scanning strategy on residual stress distribution in additively manufactured 316L steel, Opt. Laser Technol. 132 (2020) 106477.

[66] D.M. Stefanescu, M.D. Owens, A.M. Lane, T.S. Piwonka, K.D. Hayes, J.O. Barlow, Penetration of liquid steel in sand molds, part I: physics and chemistry of penetration and mathematical modeling-metal side, Trans.-Am. Foundrymens Soc. (2001) 1347–1364.